



Quantifying Uncertainty in the Scaling Laws of Porous Electro spray Emitters

Collin B. Whittaker^{*}, Alex A. Gorodetsky[†], and Benjamin A. Jorns[‡]
University of Michigan, Ann Arbor, Michigan, 48109

Uncertainty in the model parameters of several scaling laws applicable to porous electro sprays is quantified using Bayesian inference. Specifically, models describing ion current in the pure-ionic regime, jet current in the cone-jet regime, and the number of active emitter sites as a function of applied voltage are examined. Data from previously published experimental studies are used to generate posterior distributions of the model parameters. Different assignments for the uncertainty are considered where unavailable from empirical estimates. These distributions are then used in combination with the Electro spray Propulsion Engineering Toolkit (ESPET) QuickSolver to generate performance predictions with confidence intervals for a real porous emitter. The results of these analyses are compared to previously given values for the model parameters and experimental data external to the inference. The model parameters are found to be well determined by the data, with full widths at half maxima 1-2 orders of magnitude below their peaks. Predictions incorporating the posteriors are found not to agree the external data, and a lack of applicability of the ionic current model is examined as a cause. In light of this disagreement, the external data is incorporated to update the posteriors, and it is found that the ionic current scaling changes much more significantly than the other parameters, identifying it as the primary source of disagreement.

I. Nomenclature

$P()$	=	probability
X	=	data (generic)
θ	=	model parameters (generic)
I	=	background information
N	=	number of data
k	=	datum index
Y_k	=	measured datum (dependent)
x_k	=	measured datum (independent)
σ_k	=	uncertainty in datum
F_k	=	ideal (noiseless) datum
I_{ion}	=	pure-ionic regime ion current
I_{jet}	=	cone-jet regime droplet current
i	=	number of active emission sites
h	=	cone height
β	=	cone half-angle
R_c	=	radius of curvature
r_{base}	=	Taylor cone base radius
r_0	=	pore radius
$I_{ion,0}$	=	onset ionic current
ζ	=	ionic current scaling parameter
V	=	applied voltage (various)
V_0	=	onset voltage
C_R	=	dimensionless flow impedance

^{*}Ph.D Pre-Candidate, Department of Aerospace Engineering, AIAA Student Member.

[†]Assistant Professor, Department of Aerospace Engineering, AIAA Member.

[‡]Assistant Professor, Department of Aerospace Engineering, AIAA Senior Member.

K	=	conductivity
R_h	=	hydraulic impedance
ϵ_0	=	vacuum permittivity
γ	=	surface tension
ρ	=	density
(q/m)	=	charge-to-mass ratio
a	=	semi-interfocal distance
ξ	=	elliptic coordinate
η	=	hyperbolic coordinate
ϕ	=	azimuthal coordinate
η_0	=	hyperbolic coordinate of emitter
d	=	tip-to-extractor distance
μ	=	dynamic viscosity
κ	=	permeability
ϕ_p	=	porosity
α	=	cone-jet current scaling parameter
$I_{jet,0}$	=	characteristic current
Q	=	volumetric flow rate
Q_0	=	characteristic volumetric flow rate
b_0	=	pooling radius
N_{max}	=	maximum emission sites
$C_{R,limit}$	=	ESPET mode-switching limit
p_{scale}	=	ESPET pressure-scaling factor
I_{ESPET}	=	EPSET current output

II. Introduction

The electro spray thruster is a potentially revolutionizing technology for in-space propulsion. This stems from its unique principle of operation, where strong electric fields are used to extract and accelerate charged particles directly from an ionic liquid. This ability to operate on storable, ionic liquids offers advantages in terms of both system mass and efficiency compared to other state of the art (SOA) electric propulsion (EP) technologies like Hall thrusters and gridded ion thrusters [1]. Similarly, as the ionic liquid is effectively pre-ionized (requiring no ionization loss penalty), electro spray devices are able to avoid typical volume to area losses encountered by alternative forms of plasma EP devices as they are scaled down in size. This recommends electro sprays for low power, small satellite operation. In principle, these devices can also be scaled up to arbitrary power without penalty by arraying many emitters together to meet mission requirements [1–3].

There are multiple methods for creating electro sprays for propulsion. All of these methods share the common feature that a strong electric field is applied locally to the propellant surface. Charged droplets or individual ions can be extracted from the resulting electrified fluid meniscus provided this field is sufficient to overcome the cohesive forces of the liquid. An emitter with a sharp geometry to amplify the electric field to this level supplies the liquid, and a downstream electrode (the extractor) usually serves as ground. Implementations differ principally in how they deliver fluid to the tip, including capillary, externally wetted, and porous emitters. Of these, porous emitters, which wick propellant through a substrate, are attractive for several reasons. Their ability to access the high-specific impulse pure-ionic regime (PIR) can translate to fuel savings on-orbit, their process-variable pore sizing and porosity allow additional control over the emission characteristics of the spray beyond that achieved through geometry, and their ability to be shaped and machined can support rapid prototyping and manufacturing. Porous architectures have thus gained a prominent place in electro spray development [1–8], including commercial concepts from Accion Systems [9] and ENPULSION [10].

Despite the growing body of work on porous emitters, there are a number of outstanding challenges for mission infusion that have yet to be resolved. Porous emitters may have propellant that pools outside of individual pores, develop multiple emission sites (and in particular off-axis emission sites), and have hard-to-characterize hydraulic impedances [8, 11]. The uncertainty in behavior resulting from these phenomena represent barriers to implementation, particularly in making predictions for device lifetimes, which can be limited by propellant impingement [12, 13]. One strategy to address these challenges is purely empirical: constructing thruster articles, testing them directly in vacuum facilities,

and iterating on design. This strict prototyping, however, is expensive and time-consuming. To avoid these costs, we desire a modeling-based design approach that can be used to predict device performance *a priori* for a given design. In particular, we desire a strategy suited to leveraging the powerful tools of design optimization to more efficiently search the large electrospay design space.

There are several possible architectures for performing optimized, model-based design. A full kinetic model could be used to directly model the dynamics of the electrospay process, but such models are expensive to evaluate and may resolve relevant physical processes with higher fidelity than required for some design decisions. Physics-based, data-driven modeling, which leverages both first-principles understanding and the power of empirical data, is an expeditious alternative. It relies on representing key processes through simple algebraic scaling laws. These relationships are cheap to evaluate and well-suited to rapid and robust design optimization, and they provide quick ways to estimate, for example, device lifetimes. The major technical trade is that some nuances of the physics must be captured in *ad hoc* scaling coefficients which need to be calibrated against data. To date, there has been marked success in deriving a subset of scaling laws for electrospays and porous emitters (see [11, 14–19]).

The use of data-calibrated scaling laws, while effective, has a number of potential drawbacks. Many of these scaling laws have been calibrated against limited data drawn from one emitter configuration. This raises questions about their extensibility beyond the training data. Relatedly, reducing complex physics into a few model coefficients may be overly simple for some processes. Failing to account for the error engendered in this process compromises the model predictions. Additionally, these parameters may be taken to be given deterministically, which can erase relevant information by ignoring, for example, the comparative quality of data. With these limitations in mind, the need is apparent for a methodology that addresses these shortcomings.

Bayesian data analysis is well-suited to address this need. Bayesian inference allows for the rigorous characterization of uncertainty in model parameters by relating it to uncertainty in data and incorporating prior knowledge and constraints. In this work, we apply these techniques to existing scaling laws relevant to porous electrospays. To this end, this paper is organized in the following way. First, we provide a general overview of the ESPET numerical tool that we use for electrospay modeling, identifying the key submodels and scaling laws. We next provide a high-level description of the Bayesian framework and Bayesian parameter estimation and how this can be applied to calibrate models. Next, we review the models examined as a part of this study and describe the corresponding Bayesian formulations. We present the results of our analysis, generating probability distributions for each model parameter. We then use these distributions to make probabilistic predictions for an electrospay emitter that has been experimentally characterized. We use these data to refine our estimates for the model distributions and make another set of predictions for a similar electrospay. Finally, we discuss the results and the utility of the Bayesian formulation.

III. Theory and Methods

In this section we outline the methodologies underpinning our analysis and describe the models analyzed.

A. ESPET Overview

The Electrospay Propulsion Engineering Toolkit (ESPET) is a performance estimation tool for propulsive electrospay systems. It incorporates a suite of scaling laws and a database of propellant properties to provide performance predictions for a variety of popular electrospay architectures [11, 17]. For porous emitters, the ESPET QuickSolver (which we work with here) incorporates models to describe the impedance of and propellant flow through the emitter, emission onset (including of multiple sites), a hard mode switch for whether these sites are operating in a pure-ionic or cone-jet regime, and the corresponding ionic and droplet currents for each site. Some of these models, such as the ionic and cone-jet currents, are semi-empirical, with scalings either specified by the user or taken from published data. ESPET already includes tools for considering random errors in geometry (i.e. from manufacturing tolerances), and one of the goals of this work is to provide a framework through which uncertainty in the underlying models employed by ESPET can also be considered.

B. Bayesian Parameter Estimation

Bayesian parameter estimation is a technique for fitting models that employs Bayes' theorem. It is predicated on the application of Bayes' rule, which allows us to relate our degree of confidence in a set of model parameters (e.g. the

slope and offset of a line) conditional on the measured data. Formally, this is written as

$$P(\theta|X, I) = \frac{P(X|\theta, I) \times P(\theta|I)}{P(X|I)}, \quad (1)$$

where X represents the data, θ the model parameters, and I any relevant background information, with vertical bars indicating conditional probabilities. The term $P(\theta|I)$ is the prior distribution – it represents the information available about the model parameters prior to the incorporation of the data X . The term $P(X|I)$ is called the evidence and for our purposes is discarded as a normalization constant. In other problems (i.e. model selection), the evidence is paramount [20]. $P(X|\theta, I)$ is the likelihood, the conditional probability of observing the data. Finally, $P(\theta|X, I)$ denotes the posterior, a probabilistic characterization of the remaining uncertainty about the parameters following the incorporation of the data.

As an illustrative example of the application of this rule, we present the case of fitting an arbitrary model with parameters θ to N data Y_k taken at points x_k , which are assumed to be exactly known for simplicity. We suppose that the data Y_k are subject to some noise and will not follow the model exactly. We do so by assigning a Gaussian likelihood (as is often done) to each datum Y_k with uncertainty σ_k , such that

$$P(Y_k|\theta, \sigma_k, I) = \frac{1}{\sigma_k \sqrt{2\pi}} \exp \left[-\frac{(F_k - Y_k)^2}{2\sigma_k^2} \right]. \quad (2)$$

$F_k = F(x_k; \theta)$ is an ideal (noiseless) datum, simply the model evaluated at x_k using the parameters θ . The assignment of the Gaussian likelihood, then, supposes the measured datum Y_k is normally distributed about the ideal datum. If we assume that the data are independent, then the joint likelihood of the set $\{Y_k\}$ is then

$$P(\{Y_k\} | \theta, \{\sigma_k\}, I) = \prod_{k=1}^N P(Y_k | \theta, \{\sigma_k\}, I). \quad (3)$$

Applying Bayes' rule, we can therefore express the posterior distribution

$$P(\theta, \{\sigma_k\} | \{Y_k\}, I) \propto P(\{Y_k\} | \theta, \{\sigma_k\}, I) P(\theta, \{\sigma_k\} | I). \quad (4)$$

If the uncertainties are known for the measurement or assumed as part of the analysis $\sigma_k = \sigma_{k,0}$, then the corresponding prior probabilities are just delta functions $P(\sigma_k | I) = \delta(\sigma_k - \sigma_{k,0})$ and can be absorbed into the background information I :

$$P(\theta | \{Y_k\}, I) \propto P(\{Y_k\} | \theta, I) P(\theta | I). \quad (5)$$

If I contained no prior insight about θ , we could encapsulate our ignorance by assigning a uniform distribution for the prior probability:

$$P(\theta|I) = \text{constant}, \quad \theta_{min} \leq \theta \leq \theta_{max} \quad (6)$$

This form is convenient because it can be absorbed into the proportionality and eliminated from the analysis, provided the limits on the parameters θ do not significantly truncate the likelihood. If instead I contained some knowledge of θ , i.e. from previous experiment and analysis, we could incorporate this by using the posterior yielded by that analysis as a prior.

C. Scaling Laws to be Calibrated

For our analysis, we target three of ESPET's core models, namely those predicting the ionic current in the PIR, I_{ion} , the droplet current in the cone-jet regime, I_{jet} , and the number of active emissions sites for an emitter, i . We do so because these relationships are central to ESPET's overall performance estimates and are comparatively well-characterized in the literature, with some studies examining them explicitly. The ionic current model and emission sites model both incorporate, at some level, the geometry of the emitter. We consider primarily porous cone emitters in this work, so for reference we display in Fig. 1 a nominal cross-section (not to scale) with device geometries labeled, a notional Taylor cone, and a token pore.

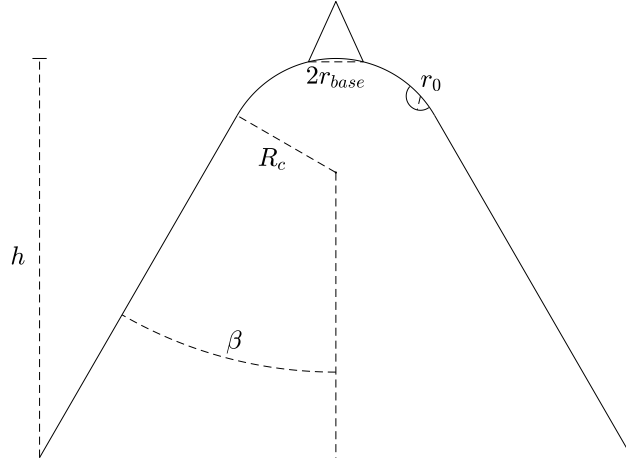


Fig. 1 Nominal cone geometry with relevant emitter geometries labeled, a token Taylor cone, and a representative pore

1. Pure-Ionic Regime Ion Current

Pure-ionic emission is a region where only ions are extracted from the emitter. This contrasts with the droplet or mixed modes where the charge-to-mass ratio is lower. Higher charge-to-mass ratios translate into higher particle exit velocities when accelerated across the potential difference of the electro spray, and therefore higher specific impulse, a key measure of fuel efficiency for propulsive systems. This makes the PIR highly attractive for these applications. Empirically, it has been found that accessing this regime requires a high level of hydraulic impedance to limit flow and prevent the formation of a cone-jet. This has been a challenge for capillary flow. Porous emitters are able to address this challenge by selecting pore size and porosity to sufficiently constrict flow through the substrate.

Transition to the PIR is not well-understood. It is unclear when it onsets and to what extent the overarching operation of the emitter determines the emission characteristics, including beam current and composition. A notional diagram in Fig. 2 illustrates the pure-ionic and cone-jet regimes. Excellent work by Coffman et al. [14, 16] has shed new light on this by considering a family of meniscus structures consistent with PIR operation. By describing the behavior of these menisci coupled with the propellant feed, they are able to provide a scaling for the current evaporated from the meniscus. We examine this model in the form presented by [11, 17] for this study.

$$I_{ion} - I_{ion,0} = \zeta \frac{V - V_0}{C_R}, \quad (7)$$

where V is the applied voltage, V_0 the emission onset voltage, I_{ion} the beam current, and $I_{ion,0}$ the beam current at onset. C_R is a dimensionless impedance given by

$$C_R = \frac{K r_{base}^{5/2} R_h}{\epsilon_0^{1/2} \gamma^{1/2} \rho (q/m)}. \quad (8)$$

r_{base} is some characteristic feature radius (which may correspond, say, to that of a pore), R_h is the hydraulic impedance, and K , γ , ρ , ϵ_0 , and (q/m) are respectively, the conductivity, surface tension, density, vacuum permittivity, and charge-to-mass ratio. We take (q/m) to be the mean charge-to-mass ratio in the spray. This relationship is derived by considering the feeding condition of the meniscus, which [14] illustrates is linked to the applied field, and by noting that the relationship appears approximately linear, as supported by experiment [2, 8, 21]. It therefore predicts a linear rise of the ionic current above some onset point $(I_{ion,0}, V_0)$ with applied voltage. This linear relationship is scaled by the dimensionless impedance C_R , and as formulated here ζ has units of inverse Ohms, therefore capturing some

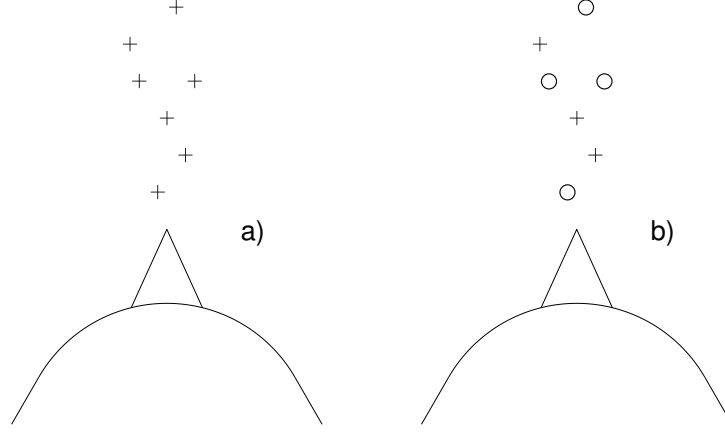


Fig. 2 a) Emitter operating in PIR $C_R > C_{R,limit}$; b) emitter operating in a mixed regime $C_R < C_{R,limit}$

characteristic resistivity. While [14] explores the solution space for these collections of menisci, simple conditions for determining the onset or transition out of this regime are not presented. For this reason, ESPET incorporates a hard mode switch limit $C_{R,limit}$ to select a relevant scaling for the operating point of interest, with $C_R > C_{R,limit}$ corresponding to the PIR, emphasizing that the hydraulic impedance must be large enough to access the PIR.

All of the parameters in Eq. 7 can be inferred directly from experiment with the exception of the slope ζ . r_{base} can be estimated from the onset voltage V_0 by approximating the emitter and extractor as confocal, equipotential hyperboloids (see [8, 11, 17, 19]). A balance between the corresponding electric field and the capillary pressure characteristic of the feature yields

$$\frac{2\gamma}{r_{base}} = \frac{1}{2}\epsilon_0 \frac{V_0^2}{a^2 \operatorname{atanh}^2(\eta_0)} \frac{1}{(1 - \eta_0^2)^2}. \quad (9)$$

Here a is the semi-interfocal distance of a system of prolate spheroidal coordinates (ξ, η, ϕ) where $\xi \in [1, \infty]$ and $\eta \in [-1, 1]$. Surfaces of η are confocal hyperboloids, with the surface $\eta = \eta_0$ approximating the emitter. a and η_0 can be related to the radius of the emitter tip R_c and emitter tip-to-extractor distance d :

$$a\eta_0 = d, \eta_0 = \sqrt{\frac{d}{d + R_c}}. \quad (10)$$

We provide an illustration of these coordinates in Fig. 3. For a given emitter and propellant, this relationship predicts that the onset voltage scales with the inverse square root of the characteristic fluid feature size (i.e. Taylor cone base radius) r_{base} , which is expected to be related to the pore size of the medium. Notably, the radii R_c and r_{base} , which determine respectively the electric and capillary pressure, are not necessarily the same for porous emitters.

The hydraulic impedance of a conical porous emitter can be estimated using Darcy's Law as:

$$R_h = \frac{\mu}{2\pi\kappa} \frac{1}{1 - \cos\beta} \left(\frac{\tan\beta}{R_c} - \frac{\cos\beta}{h} \right), \quad (11)$$

where μ is the dynamic viscosity of the propellant, β is the cone half-angle, h is the cone height, and κ is the substrate permeability, which can be determined from the pore radius r_0 and porosity ϕ_p :

$$\kappa = \frac{60 r_0^2}{(1 - \phi_p)^2}. \quad (12)$$

These equations indicate that the hydraulic impedance can be increased by lowering the pore size, increasing the porosity, increasing the sharpness of the tip (decreasing R_c), and narrowing the cone (decreasing β).

ζ is the model parameter to be calibrated. Assigning a Gaussian likelihood, the analysis proceeds as the general case treated earlier, except applied to the current data $\{I_{ion,k}\}$ and voltage data $\{V_k\}$. The corresponding ideal data are given

$$F_k = I_{ion,0} + \zeta \frac{V_k - V_0}{C_R}, \quad (13)$$

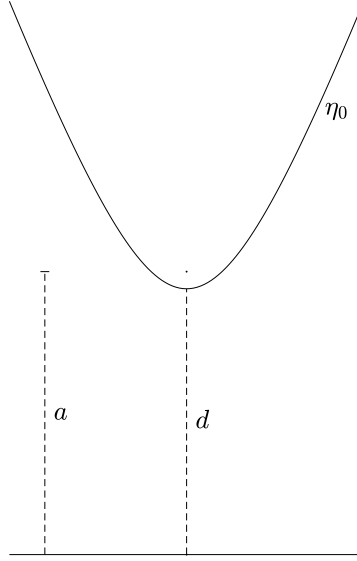


Fig. 3 Hyperboloidal geometry of Eqs. (9,10) with relevant geometric parameters labeled

resulting in the posterior distribution

$$P(\zeta | \{I_{ion,k}\}, I) \propto P(\{I_{ion,k}\} | \zeta, I) P(\zeta | I), \quad (14)$$

where the individual likelihoods are in the form of (2), the data are assumed independent, and we assign a flat prior as (6) to express our ignorance.

2. Cone-Jet Jet Current

The cone-jet regime of electro spray is characterized by the deformation of the fluid meniscus near the apex of the Taylor cone into a thin jet which carries charge away from the meniscus with current I_{jet} . It is one of the oldest known electro spray behaviors [22, 23] and has been extensively documented in the literature, as evidenced by the recent review of Gañan-Calvo et al. [18], which collects many of the scalings for cone-jet electro spray. We concern ourselves in particular with the current scaling as a function of the volumetric flow rate Q and propellant properties:

$$I_{jet} = \alpha I_{jet,0} \left(\frac{Q}{Q_0} \right)^{1/2}, \quad (15)$$

where $I_{jet,0} = \sqrt{\frac{\epsilon_0 \gamma^2}{\rho}}$ is a characteristic current and $Q_0 = \frac{\gamma \epsilon_0}{\rho K}$ is a characteristic flow rate. This scaling is determined by taking the dynamic pressure of the jet to commensurate with the electric pressure at the apex, with the radius and velocity of the jet being given by balancing the potential drop across the cone-jet transition region with the kinetic energy flux of the jet.

α is the corresponding constant of proportionality, and the model parameter to estimate in our analysis, with $\alpha = 2.6$ given in [18]. Reexamining this result within the Bayesian framework, analysis again proceeds as before, with current data $\{I_{jet,k}\}$ and flow rate data $\{Q_k\}$. The corresponding ideal data are given by

$$F_k = \alpha I_{jet,0} \left(\frac{Q_k}{Q_0} \right)^{1/2}, \quad (16)$$

with posterior distribution

$$P(\alpha | \{I_{jet,k}\}, I) \propto P(\{I_{jet,k}\} | \alpha, I) P(\alpha | I). \quad (17)$$

The data are assumed independent, the form of the likelihood is consistent with (2), and a uniform prior is chosen.

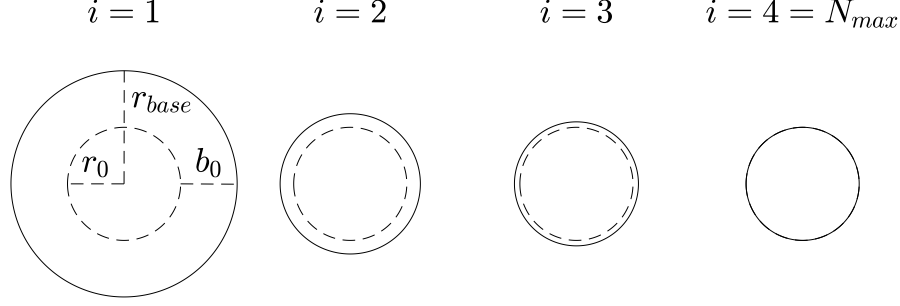


Fig. 4 Illustration of pooling model (18), with $N_{max} = 4$

3. Number of Emission Sites

A noted phenomena of porous emitters is the potential for emitters to have multiple independent emission sites [2, 6, 8, 11]. Additional sites activate as the emitter voltage is increased, a process coupled to the predicted (i.e. by (9)) pooling of propellant outside of pore sites from observations (see [8, 11]) that $r_{base} > r_0$. While experimentally verified, the onset of these additional sites is not extensively characterized. In this work, we examine a purely empirical model introduced by [11, 17].

$$r_{base} = b_0 \left[1 - \left(\frac{i-1}{N_{max}-1} \right)^{1/4} \right] + r_0, \quad (18)$$

where i is the number of active emission sites, r_0 is some feature base radius (i.e the pore size), b_0 is a pooling radius beyond the pore such that $i = 1$ corresponds to $r_{base} = b_0 + r_0$, and N_{max} is some limiting number of emission sites such that $i = N_{max}$ corresponds to $r_{base} = r_0$. This equation predicts that the effective feature size decreases as additional sites become active, as might correspond with the internal pressure of the substrate decreasing and liquid pools retreating. We show a notional diagram of this process in Fig. 4. We can rearrange this equation and solve to find a scaling law for the quantity of interest, the number of active emission sites:

$$i = (N_{max} - 1) \left(1 - \frac{r_{base} - r_0}{b_0} \right)^4 + 1, \quad (19)$$

which expresses that if we know the smallest base radius r_{base} of the emission sites, we could predict the corresponding number i .

One of the challenges of (19) is that while we can measure the number of active emission sites experimentally (see [11]), the dependent parameter, r_{base} cannot be characterized directly from experimental inspection. The features are too small and not optically accessible. To re-write this expression in terms of measurable quantities, we note that the emitter voltage may serve as an effective proxy when we consider the problem of estimating the number of sites as one of activation. To this end, we consider (9), which estimates r_{base} for a site that activates at V_0 . If we replace V_0 by the voltage of the emitter, V , we can view this expression as yielding the smallest feature that activates at a given voltage. Substituting into (19) gives the following result:

$$i = (N_{max} - 1) \left(1 - \frac{1}{b_0} \left(\frac{4\gamma a^2 \operatorname{atanh}^2(\eta_0)(1 - \eta_0^2)^2}{\epsilon_0 V^2} - r_0 \right) \right)^4 + 1, \quad (20)$$

We see that this relationship predicts the number of active emission sites will increase with applied voltage, consistent with experimental trends. Essentially, all emission sites larger than $r_{base}(V)$ activate, and then (19) describes the corresponding number of sites i .

Armed with the result in Eq. 20, we note there are two model parameters to estimate, b_0 and N_{max} . In keeping with previous analysis, for data $\{i_k\}$ and $\{V_k\}$ and assigning a Gaussian likelihood, we have ideal data:

$$F_k = (N_{max} - 1) \left(1 - \frac{r_{base,k} - r_0}{b_0} \right)^4 + 1, \quad r_{base,k} = \frac{4\gamma a^2 \operatorname{atanh}^2(\eta_0)(1 - \eta_0^2)^2}{\epsilon_0 V_k^2}, \quad (21)$$

and the (joint) posterior is simply

$$P(b_0, N_{max} | \{V_k\}, I) \propto P(\{V_k\} | b_0, N_{max}, I) P(b_0, N_{max} | I). \quad (22)$$

IV. Results

In this section, we present the results of applying Bayesian inference to the three scaling laws outlined in the preceding section. We describe the origin of the dataset and assumed error for each analysis and then present the resulting posteriors for the scaling parameters. We then use these results to try to model with uncertainty the performance of a real electrospray test article. We further update the posteriors and predictions by incorporating additional experimental data. Table 1 summarizes some elements of the inference.

Table 1 Summary of inference data and models

Model	Independent Data	Dependent Data	Parameters	Data Source
Ionic Current	Applied Voltage V_k	Ionic Current $I_{ion,k}$	ζ	Perez-Martinez [8]
Droplet Current	Flow Rate Q_k	Droplet Current $I_{jet,k}$	α	Gañan-Calvo et al. [18]
Number of Emission Sites	Applied Voltage V_k	Number of Sites i	b_0, N_{max}	St. Peter et al. [11]

A. Model Parameter Estimation

In this subsection we discuss the posterior distributions for each model examined as part of this study. Particular attention is paid to their shapes (i.e. unimodality, multimodality) and widths.

1. Pure-Ionic Regime Ion Current

We apply our earlier analysis using data reported by Perez-Martinez [2, 8] for a pair of carbon xerogel-based conical emitters operating on the ionic liquid 1-ethyl-3-methylimidazolium tetrafluoroborate (EMI-BF₄) in the pure-ionic regime. $I_{ion,0}$, V_0 , and σ_k are reported for all data used. C_R is not given directly and is therefore inferred as described previously. We restrict our analysis to those data taken in positive polarity operation, for which time-of-flight traces are provided and can be used to estimate (q/m) . We show the data used for this analysis, their experimentally-estimated uncertainties, and our most probable fit in Fig. 6.

In Fig. 5, we display the posterior probability density function (PDF) for the pure-ionic regime current scaling parameter ζ (solid line) along with the uniform prior considered (dotted line). Since the posterior has only one dimension, we determine it directly by calculating the likelihood at a large number of points within the bounds of the uniform prior and then normalizing the PDF such that it integrates to unity over the interval. We operate with the logarithm of the likelihood for the intermediate calculations to avoid numerical errors. The bounds of the prior correspond with the bounds of the figure, $P(\zeta|I) = \mathcal{U}[1.3 \times 10^{-8}, 1.5 \times 10^{-8}]$. We initially used broader limits for the prior, given by solving (deterministically) the model (7) for ζ on a datum-by-datum basis and taking the minimum and maximum of these individual predictions as the bounds of the prior. We subsequently reduced the bounds of the prior for clarity without significantly truncating the posterior. The PDF is unimodal, with a single peak (the mode) at $\zeta = 1.41 \times 10^{-8}$ and a full width at half maximum (FWHM) of 3.5×10^{-10} , or approximately 2.5%. Data corresponding to the two emitters is clearly distinguishable in Fig. 6, suggesting that the scaling may be fundamentally different between them. For completeness, then, we also show the 5th percentile, median, and 95th percentile scalings (in dotted, dash-dotted, and dotted lines, respectively) determined by applying this analysis to the two emitters individually.

2. Cone-Jet Jet Current

We conduct the cone-jet analysis using most of the data reported in [18], but some data difficult to extract from published sources are excluded. The uncertainties $\{\sigma_k\}$ are largely unreported for these data, and so we consider a few assignments for the uncertainty: first, a blanket uncertainty of 10% of the measurement, $\sigma_k = I_{jet,k} \times 10\%$; next, a blanket uncertainty of 20% of the measurement, $\sigma_k = I_{jet,k} \times 20\%$; and lastly, a uniform uncertainty equal in magnitude to the minimum datum $\sigma_k = (I_{jet,k}/I_0)_{min}$. We display the data used and the most probable fits for each of these assumptions in Fig. 8.

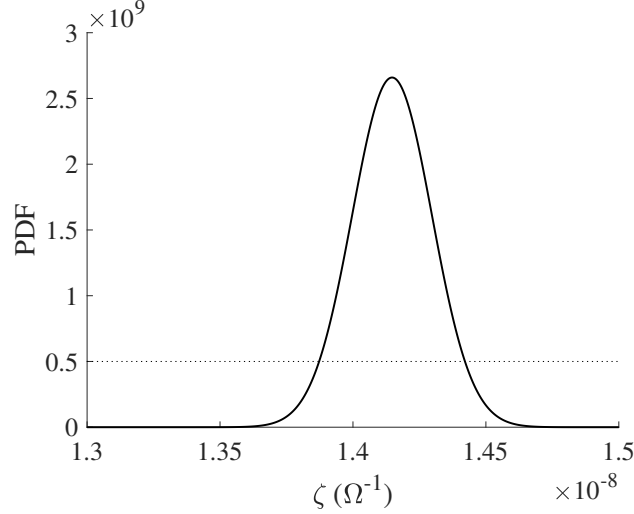


Fig. 5 Posterior PDF (solid) for ζ generated using the data of [2, 8]; also shown is the uniform prior (dotted)

In Fig. 7, we show the posterior PDFs for the parameter α of the current scaling (15), labeled by assumption. We also display (as a delta function) the scaling given by Gañan-Calvo. The limits of the prior are again consistent with the figure, $P(\alpha|I) = \mathcal{U}[1.8, 2.8]$, where we narrowed the prior without appreciably truncating the posterior similar to as was done for the PIR posteriors. The 10% uncertainty distribution has a peak at $\alpha = 1.97$, with a FWHM of 0.037, or 1.9%. The 20% posterior has its peak also at $\alpha = 1.97$ but is broader, with a FWHM of 0.073, or 3.7%. These two peaks are significantly lower than the scaling of Gañan-Calvo and indeed indicate very little confidence in such a result. The uniform uncertainty posterior, however, has a peak at $\alpha = 2.64$, which much more closely matches [18]. It has a FWHM of 0.041, or 1.6%. All four of these scalings are plotted in Fig. 8, with line styles mimicking that of Fig. 7. The two $\alpha = 1.97$ lines entirely overlap, and the $\alpha = 2.64$ line is nearly coincident with that of Gañan-Calvo on the scale of the figure.

3. Number of Sites

We apply our site model analysis to data reported in [11] for the operation of a conical porous borosilicate emitter using 1-ethyl-3-methylimidazolium bis(trifluoromethylsulfonyl)imide (EMI-TFSI), in both the positive and negative polarity. No uncertainty is reported for these measurements, and so an uncertainty equal in magnitude to the minimum datum is assigned, $\sigma_k = \min(i_k)$, motivated by our earlier results for the cone-jet current scaling. A flat prior is used. The data used to calibrate the model are shown in Fig. 10, along with, from lowest to highest, the 5th percentile, median (solid), and 95th percentile predictions from sampling the posterior and evaluating over the domain (see IV.B for additional information).

We plot in Fig. 9 three key results of the parameter estimation for b_0 and N_{max} . Again, the prior is uniform $P(b_0, N_{max}|I) = \mathcal{U}_{b_0}[6.5 \times 10^{-6}, 12.5 \times 10^{-6}] \mathcal{U}_{N_{max}}[10, 35]$. On the bottom left is a contour plot of the unity-normalized joint posterior PDF. The PDF has a single banana-shaped bump with a maximum at $(b_0, N_{max}) = (9.011 \times 10^{-6}, 22.46)$. The shape of the contours indicate that there is significant and nontrivial correlation between b_0 and N_{max} , with a rise in N_{max} implying a decrease in b_0 . We discuss the physical implications of this further in Sec. V. In the top left is a marginal distribution for b_0 , that is, the (1D) distribution without regard to N_{max} :

$$P(b_0|\{i_k\}, I) = \int P(b_0, N_{max}|\{i_k\}, I) dN_{max}. \quad (23)$$

It has a slightly different maximum, at $b_0 = 8.914 \times 10^{-6}$, and a FWHM of 1.813×10^{-6} , or 20.3%. The rightmost plot is instead the marginal distribution for N_{max} . It has a maximum at $N_{max} = 22.04$, with a FWHM of 6.36, or 28.9%. These marginal distributions are broader than any of those of the two current scaling laws. Their correlation also suggests that there exists a combination of these two parameters that is determined better than either of them individually and the potential for a physical link.

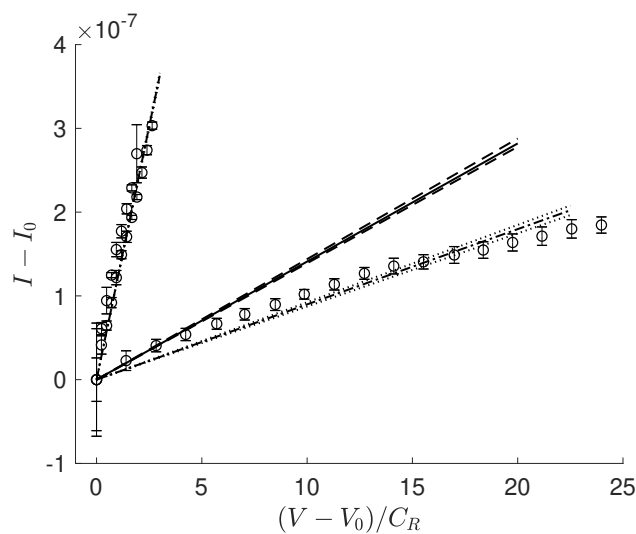


Fig. 6 Data extracted from [8] for emitters operating in the PIR, with error bars equal to σ_k (given by empirical estimate) on either side; the solid line is the most probable estimate, and the dashed lines at the 5th and 95th percentiles; also shown are 5th percentile, median, and 95th percentile scalings for individual emitters, in dotted, dash-dotted, and dotted lines, respectively.

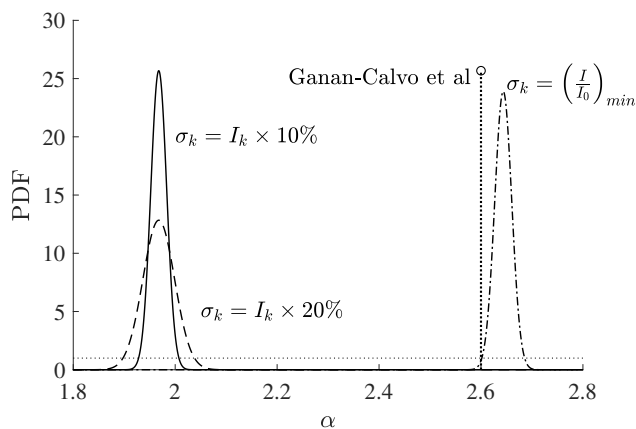


Fig. 7 Posterior PDFs for various assignments of the uncertainty alongside the scaling of [18]; the light dotted line is the uniform prior

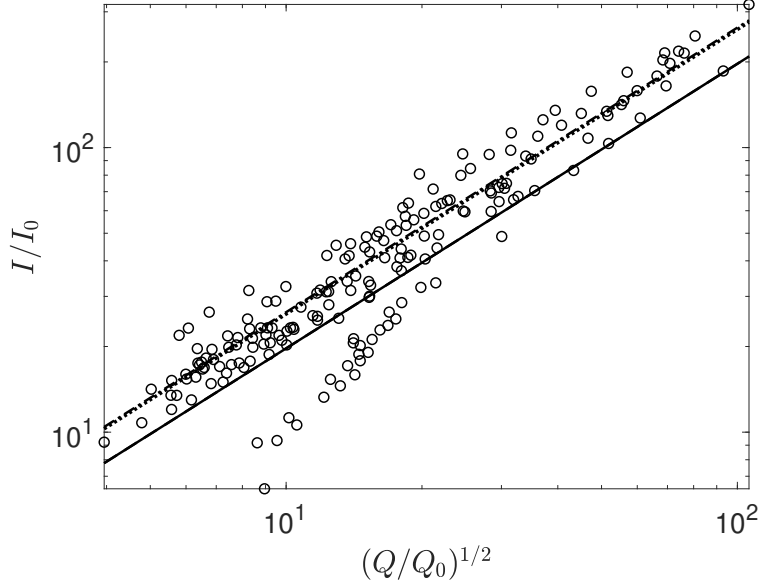


Fig. 8 Data and inferred α for three different uncertainty assignments: 10% of measurement (solid line), 20% of measurement (dashed line), and equivalent to minimum datum (dash-dotted line) alongside the scaling of [18] (dotted line)

B. Model Predictions with Confidence

As a practical example of the utility of the posterior distributions generated, we make probabilistic performance predictions for a real electrospray test article. We consider the borosilicate emitter which provided the training data for the emission sites model, whose relevant features are described in [11]. Presented there also are experimental I-V curves, which offer a useful comparison. Our performance predictions are made as follows. First, the posterior distributions of Figs. 5, 7, and 9 are each sampled 10000 times. The sampling is straightforward for the ζ and α distributions, but the correlation between b_0 and N_{max} means that sampling these parameters independently from their marginal PDFs would not be representative of the joint PDF. Instead, we make a draw by first sampling the marginal b_0 PDF, then sampling the conditional PDF $P(N_{max}|b_0)$ (i.e. the corresponding slice of the joint PDF). This provides a linked pair of the two parameters. After generating these samples, we run the ESPET QuickSolver 10000 times for the emitter, with voltage as an independent variable and each run using a different parameter set. Parameters for other models contained in ESPET not examined by this study are chosen to be consistent with [11]; we collect these and the relevant geometries of the emitter in Table 2. These model evaluations thus produce 10000 different I-V curves and therefore 10000 current predictions at each voltage setpoint. For sampling α , we elect to use distribution corresponding to the flat uncertainty assignment, a decision motivated later. We display the predictions produced with this method in Fig. 11. The solid black line is the median predicted current at each setpoint, the dashed lines are the 33rd and 66th percentiles, and the dotted lines are the 5th and 95th percentiles.

There are several discontinuities evident in the plot. As noted by [11], these are due to discrete elements of the QuickSolver, namely the onset of additional emission sites and the hard mode-switching limit between the pure-ionic regime of (7) and the cone-jet regime of (15). The width of these discontinuities evidenced by the confidence bounds suggests a lack of certainty in the location of these transitions, i.e. some sets of parameters resolve to one side of each discontinuity and some to the other, but the balance shifts over the transition. This behavior is most pronounced in the higher-voltage regime.

We also show in Fig. 11 a comparison of these same predictions to the experiments of [11] on the emitter described in Table 2 operating on EMI-TFSI. The predictions from the Bayesian calibrated model fall notably below the experimental data. This discrepancy is about a factor of three across the domain. We discuss possible reasons for this discrepancy in Sec. V.

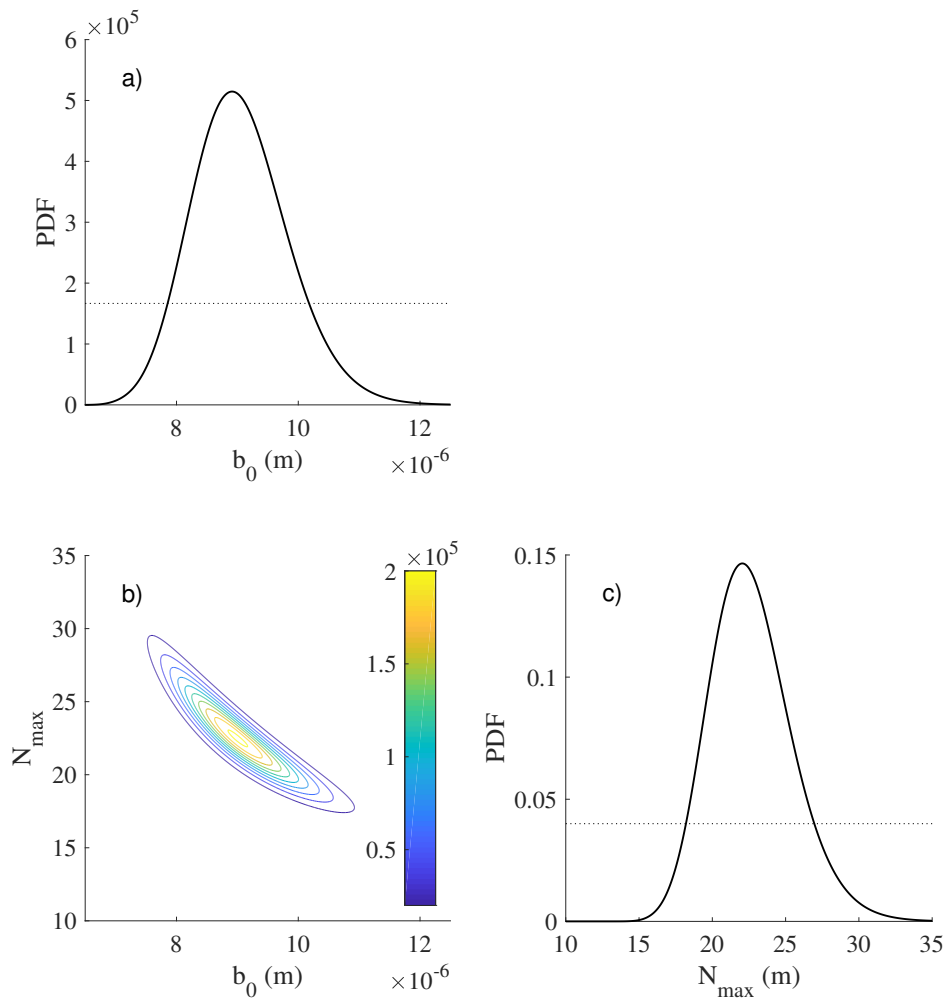


Fig. 9 a) marginal b_0 PDF; b) Contour plot of the (b_0, N_{max}) joint PDF for emission site data reported by [11]; c) marginal N_{max} PDF; priors are shown as dotted lines

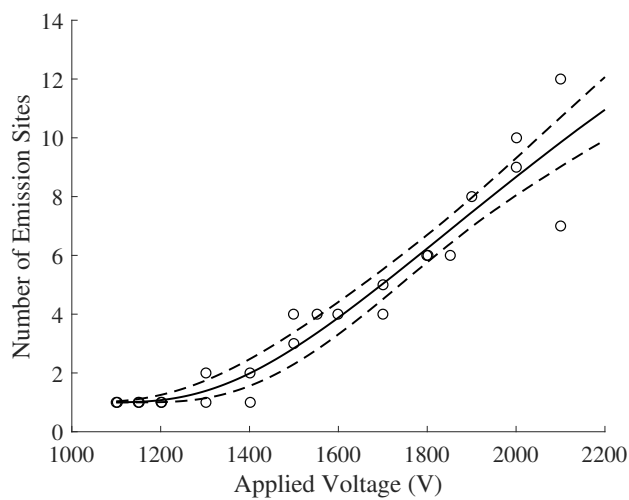


Fig. 10 Calibration data for the emission site activation model and the 5th percentile (lower dashed), median (solid), and 95th percentile prediction; uncertainty equal in magnitude to the minimum datum is assumed

Table 2 Collection of relevant ESPET properties and parameters for our probabilistic predictions

Property	Value
h (m)	3.5×10^{-4}
β (deg)	30
R_c (m)	16×10^{-6}
r_0 (m)	6.5×10^{-7}
ϕ_p	0.5
d (m)	1.2×10^{-4}
Parameter	Value
$C_{R,limit}$	20
p_{scale}	0.023
Spray divergence (deg)	30

C. Updating coefficient posteriors with new data

The modeling predictions from Fig. 11 suggest that the posteriors we have generated from calibrating the individual scaling laws do not lead to model predictions consistent with experimental data. There are a number of possible explanations for this, including the possibility that the scaling laws do not extend to this thruster geometry or that the model parameters are correlated. With this in mind, one of the most powerful capabilities of the Bayesian method is that it allows us to update our knowledge of the model parameter distributions in light of new data.

To this end, we use the dataset from Fig. 11 in a new formulation of Bayes' rule

$$P(\zeta, \alpha, N_{max}, b_0 | \{V_k, I_k\}) \propto P(\{V_k, I_k\} | \zeta, \alpha, N_{max}, b_0) P(\zeta) P(\alpha) P(N_{max}, b_0), \quad (24)$$

where we have used the posteriors determined from the previous sections (Eq. 14,16, etc.). In this case we define

$$F_k = I_{ESPET}(V_k | \zeta, \alpha, N_{max}, b_0) \quad (25)$$

where I_{ESPET} is the current predicted by the ESPET model. We draw 10000 samples from this posterior by implementing a Markov Chain Monte Carlo (MCMC) sampler. Since under our assumption of independent data there is no difference between analyzing these data sequentially or all at once, for practical purposes we treat this as a single inference in light of all data. We assign a flat uncertainty for the ESPET-predicted data consistent with previous analyses, but change the magnitude of the uncertainties used (including those taken from experiment) such that they are on the same order relative to their respective data due to problems with the sampler. These can be found in the appendix. We show in Fig. 12 the posterior distributions of the coefficients. The diagonals are the four marginal distributions corresponding to the labels along the bottom. The 2D histograms are the marginal joint PDF of the two variables that intersect at that coordinate. These posteriors are very similar to those obtained previously, except that there has been a notable shift (about 15%) upward in the ζ distribution. We display in Fig. 13 the revised model predictions and their confidence intervals. These predictions still largely disagree with experiment, but match more closely than before, as the increase in predicted ζ values corresponds to an increase in the predicted current.

Noticing the primary change has been in ζ and the potential problems of the data in Fig. 6, we make another set of predictions where we neglect these data and their corresponding inference entirely, taking the prior $P(\zeta)$ of Eq. (24) to be uniform instead. These results, in the form of the updated posteriors and predictions shown in similar style as previously, are shown, respectively, in Figs. 14 and 15. The b_0 , N_{max} , and α posteriors are again very similar to previous, but the ζ distribution has been allowed to change, now peaked near $\zeta = 5.71 \times 10^{-8} \Omega^{-1}$. Additionally, the predictions show much closer agreement with experiment. This is unsurprising because our inference about ζ is now given entirely by the experimental data shown in Figs. 11, 13, and 15.

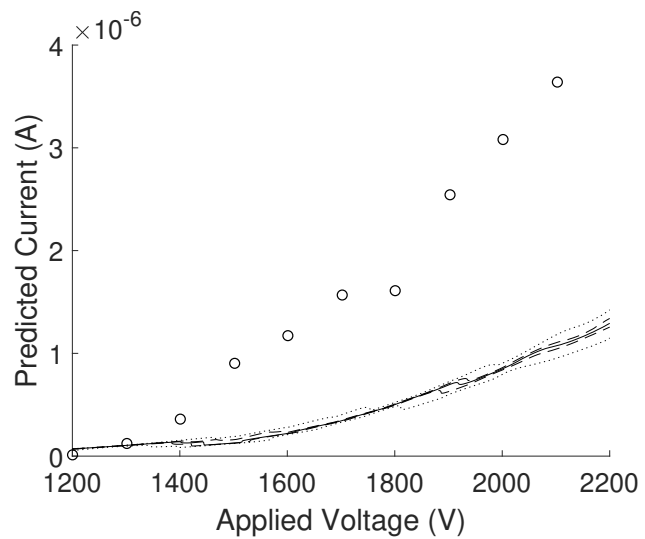


Fig. 11 Probabilistically-predicted current-voltage curves compared to experiments [11]; median prediction (solid), 33rd and 66th percentiles (dashed), 5th and 95th percentiles (dotted)

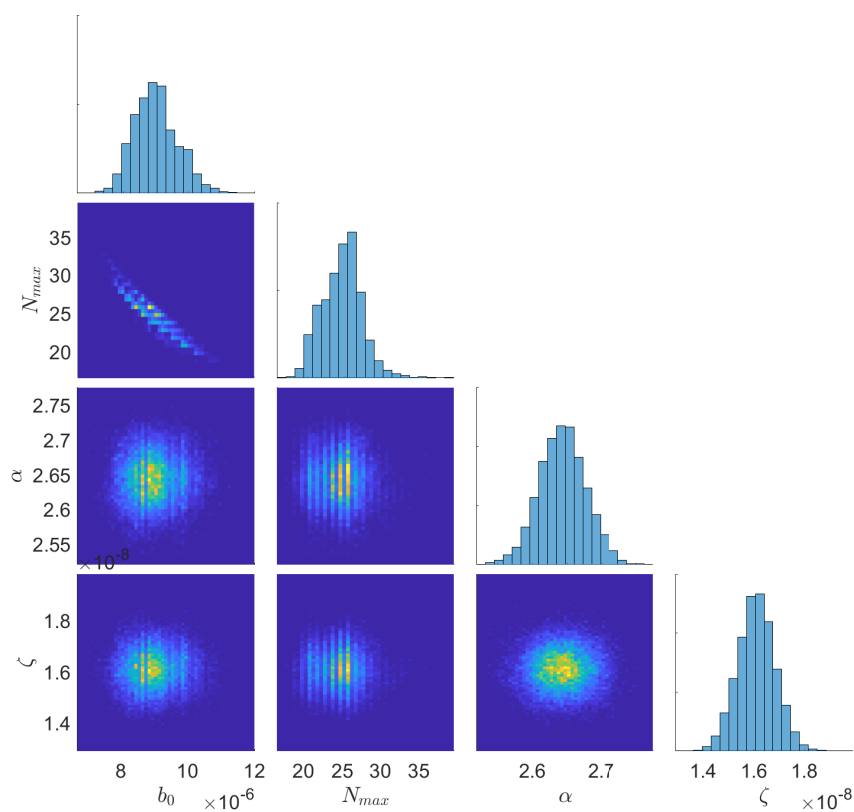


Fig. 12 Revised posterior distributions generated by MCMC sampling; diagonal entries are marginal distributions corresponding to the labels on the bottom, and non-diagonal entries are the marginal joint distribution of the two intersecting parameters

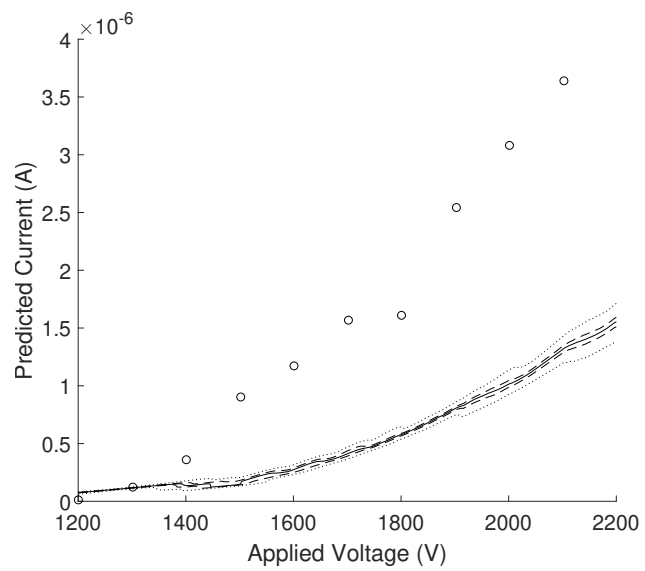


Fig. 13 Updated performance predictions using experimental data of [11]

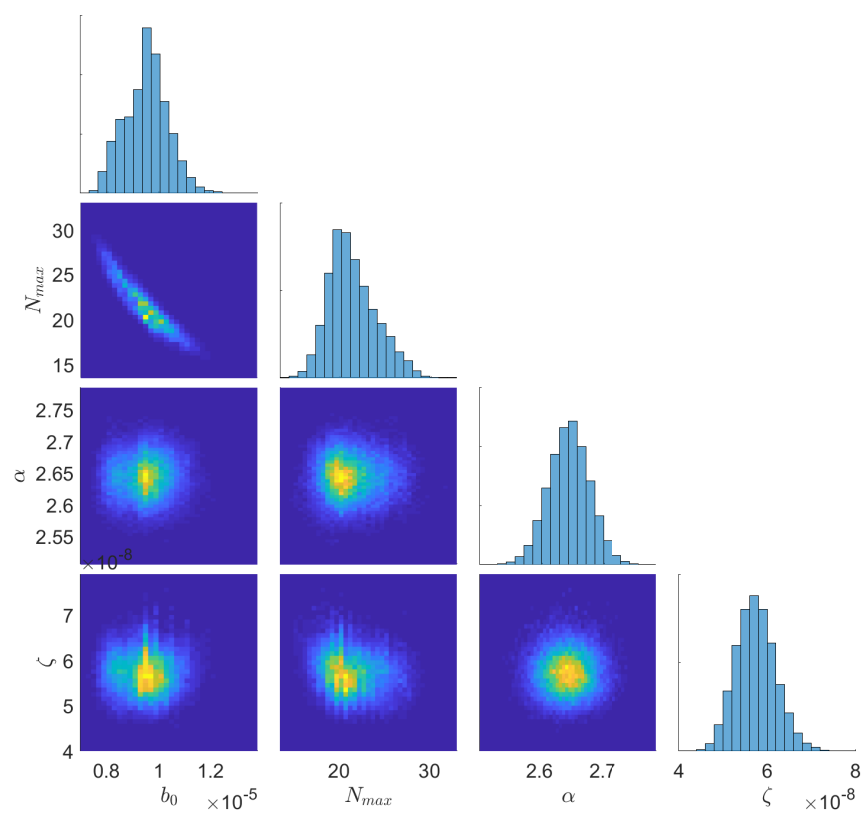


Fig. 14 Posterior distribution using the data of [11] and neglecting previous ζ inference

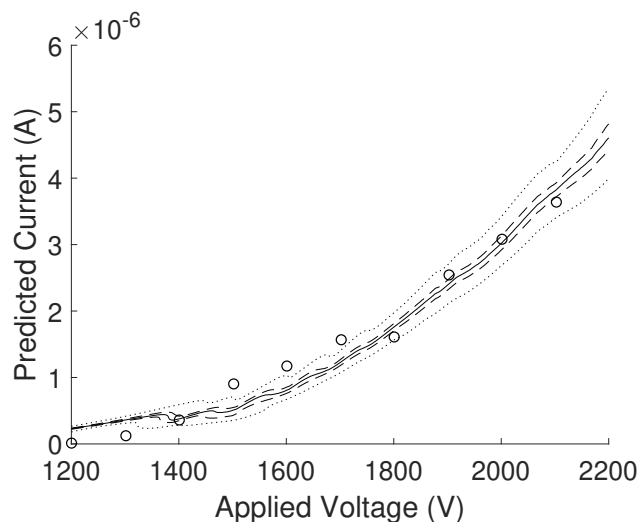


Fig. 15 Performance predictions neglecting the data of Fig. 6.

V. Discussion

A. Impact of experimental error on posterior distribution of droplet spray scaling law

We begin by discussing the impact of the assumption of error when unavailable from data. We presented in Figs. 7 and 8 three different choices for the uncertainty: 10%, 20%, and equal to the minimum datum. As previously noted, there is considerable disagreement between those posteriors for which we assumed an uncertainty proportional to the data and the deterministic value quoted by Gañan-Calvo et al. This is an interesting and surprising result. We might expect a proportional uncertainty to be physically reasonable, inasmuch as we would not expect to resolve measurements on the order of megaAmperes to picoAmpere precision. However, if we assign a proportional uncertainty, we implicitly take data at lower values to be better specified. This may not be reasonable if data of different magnitude were captured with similar precision (e.g. by the same or similar instruments), which is probable. This difficulty emphasizes that due consideration must be afforded to the uncertainty in the data when no immediate assignment is available (i.e. from experiment or instrument calibrations). These considerations motivated the subsequent application of a flat uncertainty to further analysis.

B. Limitations of pure-ionic scaling law

The results for the pure-ionic regime ion current are not as much subject to these ambiguities, as they are taken from experimentally-estimated uncertainties. However, they failed to predict the I-V curve of a real electrospray when used in conjunction with other analyses, underestimating the emitted current across the domain. This discrepancy may be largely attributed to the ζ probability distribution. When [11] benchmarked ESPET directly against the same experimental data, they used a value of ζ about 3 times greater than that predicted initially here. This deficit corresponds closely to the deficit in predicted current. A perfunctory examination of the ESPET results also reveals that over much of the prediction domain, a majority of emission sites are operating in the ionic regime, suggesting that this scaling may have an outsize role in these predictions. Indeed, when we updated the posterior distributions for the model coefficients in light of the data in Fig. 11, we found that ζ adjusted to higher values while the other coefficient distributions remained approximately the same. This suggests, within the limited scope of those data, that the parameter ζ may not be universal among electrosprays—even for comparatively similar emitters, as we noted of Fig. 6.

C. Correlation between model coefficients in model for active emission sites

The joint b_0, N_{max} posterior shows quantitative agreement with the choices of [11], which were benchmarked to the same data using ESPET. The correlation between these two parameters suggests a physical link between them, which seems intuitively reasonable insofar as N_{max} is taken to represent some limit to the number of sites which can develop. We would expect the effective area over which propellant could pool to be related to the device geometry, particularly

the size or curvature of the tip, which we would also expect to play a determining role in the maximum number of emission sites.

D. Implications of Bayesian inference for robust design and optimization

The probabilistic predictions described in this work provide an example of the usefulness of the Bayesian formulation. By not taking model parameters to be deterministic from data, we have allowed the uncertainty in the data to inform uncertainty in the parameters themselves. That is, there is not one right answer, but a family of variably plausible ones. Properly treating this variability can provide more comprehensive predictions. An illustrative example is the problem of predicting the performance of an array of emitters. Each emitter is subject to uncertainty in its performance. This uncertainty can come from several sources: uncertainty in its construction (ideally captured by manufacturing tolerances), uncertainty in its operation (i.e. the mapping between control inputs and operational parameters), and uncertainty in its behavior (ideally captured by the kind of analysis described here). If we rigorously account for these, we can describe the performance of the array as a whole by considering it probabilistically. This opens additional avenues to performing robust design optimization, and, provided the predictions are sufficiently accurate, could preempt the need for direct testing.

Additionally, this analysis is useful for future model development and can provide new physical insights. We noted already the evident disagreement over ζ . This would tend to indicate a deficiency in the model. We note, though, that application of this model required estimation of the quantities r_{base} and R_h , which may not be easily determined in their own right. A more successful application of the scaling (7) to our problem could simply require a more rigorous description of these quantities (i.e. more modeling). As a further example of physical insight, we consider again Fig. 11. Though not necessarily evident in the figure, the discontinuities correspond to multimodality in the predictions, with sometimes a handful of comparably plausible populations. This may indicate the presence of multistable emission modes, particularly in the higher-voltage regime.

VI. Conclusion

In summary, we have used Bayesian methods to rigorously account for uncertainty in fit parameters for a number of scaling laws applicable to porous electrosprays, in particular those describing ion current in the pure-ionic regime, droplet current in the cone-jet regime, and the number of active emitter sites as a function of voltage. We found the posterior distributions for the ionic and cone-jet scalings to be well determined by the data used, but discuss potential limitations and possible extensions. We then used these results to make probabilistic predictions for a real emitter by constructing and evaluating sets of parameters using the ESPET QuickSolver. These predictions provide a detailed description of the conclusions of their constituent models. We found significant disagreement between our predictions and experimental data, but were able to update our inferences in light of these data and provide revised predictions that corresponded more closely.

These results are encouraging for the further development of these techniques and for their incorporation into efficient engineering tools like ESPET. With additional relevant data, we can expect this predictive capability to grow further, laying a foundation of uncertainty quantification to support the powerful tools of robust design optimization, which are better suited to tackling the large design space of electrospray propulsion than direct prototyping. Addressing this challenge is a critical milestone in transitioning electrospray thruster concepts to higher powers, allowing their revolutionary performance potential to play out on the wider stage.

Appendix

Table 3 Uncertainties used for the analysis of Figs. 13 and 15

Data	Uncertainty σ_k
PIR Data $I_{ion} - I_{ion,0}$ (Fig. 6)	5x experiment
Cone-Jet Data $I_{jet}/I_{jet,0}$ (Fig. 8)	12.49
Sites Data i (Fig. 10)	.966 sites
Operation Data I (Fig. 11)	3.48×10^{-7} Amperes

Acknowledgments

This work was supported by an Early Stage Innovations grant from NASA's Space Technology Research Grants Program. We thank Mr. Benjamin St. Peter and Dr. Rainer Dressler of Spectral Science, Inc. for their continued work on ESPET and their many illuminating discussions, Dr. John Yim from NASA Glenn Research Center, Peter Dahl for his help in extracting and collecting the training data used in this study, and Audelia Szulman for her help in configuring and running ESPET.

References

- [1] Lozano, P. C., Wardle, B. L., Moloney, P., and Rawal, S., "Nanoengineered thrusters for the next giant leap in space exploration," *MRS Bulletin*, Vol. 40, No. 10, 2015, p. 842–849.
- [2] Perez-Martinez, C., and Lozano, P., "Ion field-evaporation from ionic liquids infusing carbon xerogel microtips," *Applied Physics Letters*, Vol. 107, No. 4, 2015, p. 043501.
- [3] Rojas-Herrera, J., Jivanescu, I., Freeman, D., Krejci, D., Fucetola, C., and Lozano, P., "Porous Materials for Ion-Electrospray Spacecraft Microengines," *Journal of Nanomechanics and Micromechanics*, Vol. 7, No. 3, 2017, p. 04017006.
- [4] Krejci, D., Mier-Hicks, F., Fucetola, C., Lozano, P., Schouten, A. H., and Martel, F., "Design and Characterization of a Scalable Ion Electrospray Propulsion System," *International Electric Propulsion Conference*, 2015, p. 149.
- [5] Brikner, N. A., "On the Identification and Mitigation of Life-limiting Mechanisms of Ionic Liquid Ion Sources Envisaged for Propulsion of Microspacecraft," Ph.D. thesis, Massachusetts Institute of Technology, 2015.
- [6] Courtney, D. G., "Ionic Liquid Ion Source Emitter Arrays Fabricated on Bulk Porous Substrates for Spacecraft Propulsion," Ph.D. thesis, Massachusetts Institute of Technology, 2011.
- [7] Arestie, S. M., "Porous Material and Process Development for Electrospray Propulsion Applications," Master's thesis, Massachusetts Institute of Technology, 2014.
- [8] Perez-Martinez, C. S., "Engineering Ionic Liquid Sources for Ion Beam Applications," Ph.D. thesis, Massachusetts Institute of Technology, 2016.
- [9] Accion Systems, I., "TILE: Tiled Ionic Liquid Electrospray," Web, 2019. URL <https://www.accion-systems.com/tile>.
- [10] Schönherr, T., Little, B., Krejci, D., Reissner, A., and Seifert, B., "Development, Production, and Testing of the IFM FEPP Thruster," *International Electric Propulsion Conference*, 2019, p. 362.
- [11] St.Peter, B., Dressler, R. A., Chiu, Y.-H., and Fedkiw, T., "Electrospray Propulsion Engineering Toolkit (ESPET)," *Aerospace*, Vol. 7, No. 91, 2020.
- [12] Thuppal, A., Wright, P. L., and Wirz, R. E., "Lifetime Considerations and Estimation for Electrospray Thrusters," *AIAA Propulsion and Energy Forum*, 2018, p. 4652.
- [13] Wright, P. L., Thuppal, A., and Wirz, R. E., "Life-Limiting Emission Modes for Electrospray Thrusters," *AIAA Propulsion and Energy Forum*, 2018, p. 4726.
- [14] Coffman, C., Martinez-Sanchez, M., Higuera, F., and Lozano, P. C., "Structure of the menisci of leaky dielectric liquids during electrically-assisted evaporation of ions," *Applied Physics Letters*, Vol. 109, No. 23, 2016, p. 231602.
- [15] Higuera, F. J., "Model of the meniscus of an ionic-liquid ion source," *Phys. Rev. E*, Vol. 77, 2008, p. 026308.
- [16] Coffman, C., "Electrically-Assisted Evaporation of Charged Fluids: Fundamental Modeling and Studies on Ionic Liquids," Ph.D. thesis, Massachusetts Institute of Technology, 2016.
- [17] Dressler, R. A., and St.Peter, B., *Electrospray Propulsion Engineering Toolkit, ESPET 1.0*, Spectral Sciences, Inc., 2018.
- [18] Gañán-Calvo, A. M., López-Herrera, J. M., Herrada, M. A., Ramos, A., and Montanero, J. M., "Review on the physics of electrospray: From electrokinetics to the operating conditions of single and coaxial Taylor cone-jets, and AC electrospray," *Journal of Aerosol Science*, Vol. 125, 2018, pp. 32 – 56.
- [19] Martinez-Sanchez, M., "Lecture 23-25: Colloidal Engines," Web, 2004. URL https://dspace.mit.edu/bitstream/handle/1721.1/100855/16-522-spring-2004/contents/lecture-notes/lecture23_25.pdf, lecture notes.

- [20] Sivia, D. S., and Skilling, J., *Data Analysis: A Bayesian Tutorial*, 2nd ed., Oxford Science Publications, 2006.
- [21] Legge, R. S., and Lozano, P. C., “Electrospray Propulsion Based on Emitters Microfabricated in Porous Metals,” *Journal of Propulsion and Power*, Vol. 27, No. 2, 2011, pp. 485–495.
- [22] Zeleny, J., “The electrical discharge from liquid points, and a hydrostatic method of measuring the electric intensity at their surfaces,” *Physical Review*, Vol. 3, No. 2, 1914, pp. 69–91.
- [23] Zeleny, J., “Instability of electrified liquid surfaces,” *Physical Review*, Vol. 10, No. 1, 1917, pp. 1–10.